





Advanced method for electrical characterization of carrier-selective passivating contacts using transfer-length-method measurements under variable illumination

Cite as: J. Appl. Phys. **129**, 195707 (2021); doi: [10.1063/5.0042854](https://doi.org/10.1063/5.0042854)

Submitted: 4 January 2021 · Accepted: 27 April 2021 ·

Published Online: 21 May 2021



L.-L. Senaud,^{1,2,a)}  P. Procel,^{3,4} G. Christmann,¹ A. Descoedres,¹  J. Geissbühler,¹ C. Allebé,¹ N. Badel,¹ P. Wyss,¹ M. Boccard,²  O. Isabella,³ M. Zeman,³ S. Nicolay,¹ M. Despeisse,¹ C. Ballif,^{1,2}  and B. Paviet-Salomon¹

AFFILIATIONS

¹CSEM PV-Center, Rue Jaquet-Droz 1, CH-2002 Neuchâtel, Switzerland

²EPFL, Photovoltaics and Thin Film Electronics Laboratory, Rue de la Maladière 71b, CH-2000 Neuchâtel, Switzerland

³PVMD, Delft University of Technology (TU Delft), Mekelweg 5, 2628 CD Delft, The Netherlands

⁴Instituto de Micro y Nanoelectrónica—Universidad San Francisco de Quito, Diego de Robles s/n, Quito 170901, Ecuador

^{a)}Author to whom correspondence should be addressed: laurie-lou.senaud@csem.ch

ABSTRACT

Carrier-selective passivating contacts have been demonstrated to be crucial to reach the practical efficiency limit of single junction, crystalline silicon (c-Si) based solar cells. Yet, the electrical transport losses affecting the collection of photogenerated carriers remain to be addressed. To this aim, different methodologies and characterization techniques are currently used. In this contribution, we propose the concept of shell as a new terminology to describe carrier-selective passivating contacts. Then, we present a novel characterization methodology using transfer length method (TLM) measurement under variable illumination to investigate the charge-carrier transport in amorphous/crystalline silicon heterojunction (SHJ) n-type contact stacks. We use technology computer-aided design simulation to model a TLM structure and to identify the physical phenomena and the key parameters affecting the contact resistivity (ρ_c) and the charge carrier accumulation of such contact stacks. Then, the simulation results are compared with experimental data by performing variable-illumination TLM measurements of actual SHJ n-type contact stacks. Specifically, we demonstrate that illumination has a strong impact on the measured ρ_c value, highlighting the importance of measuring ρ_c under maximum power point conditions for a relevant characterization of solar cell transport losses. In addition, we investigate the dependence of ρ_c to a change in the injected carrier density within the c-Si bulk to compare the illumination responses of different SHJ n-type contact stacks. In the quest for maximal efficiency, this method may insightfully complete other characterization techniques to further understand and study the electrical transport in solar cells.

Published under an exclusive license by AIP Publishing. <https://doi.org/10.1063/5.0042854>

I. INTRODUCTION

The use of carrier-selective passivating contacts has been theoretically identified¹ and experimentally demonstrated^{2,3} to be the most promising way to reach the practical efficiency limit of single junction, crystalline silicon (c-Si) based solar cells. One way to overcome the remaining efficiency losses is to mitigate the transport losses affecting the extraction of photogenerated carriers⁴ by improving the passivation quality and by reducing the resistive losses, both resulting in an improvement in the overall selectivity of

the so-called *contacts* of solar cells.⁵ Along these lines, this paper is split into two main parts. In the first one, we present a generalized and unambiguous description of contacts in solar cells by introducing the terminology of *shell*.⁶ This aims to accurately investigate—and eventually mitigate—the electrical and the optical losses affecting state-of-the-art solar cells. Importantly, this terminology helps to go beyond the limitations of the term of *contacts*, which is indifferently used to refer to any part of the solar cell where the generated carriers are extracted, and, therefore, to

precisely consider the interface and the physical property coupling present between the different material layers in solar cells. In the second part, we present a novel characterization method based on an upgraded theoretical framework of transfer length method (TLM) measurements. To characterize the resistive losses of contact stacks, the TLM measurement has been widely used to determine their contact resistivity (ρ_c) and, thus, to quantify their electrical losses once integrated in solar cells. Currently, however, ρ_c measurements are performed under dark conditions and, thus, do not consider the impact of the injection present inside the c-Si bulk on electrical transport quality. In this work, we use TLM measurements under variable illumination to further study specific shells including different electron-collecting contact stacks in the amorphous/crystalline silicon heterojunction (SHJ) technology.⁷ Using this improved characterization method, we demonstrate (i) that illumination, and, thus, the injected carrier density inside the c-Si bulk, has a strong impact on the ρ_c value, (ii) the importance of measuring ρ_c under maximum power point (MPP) conditions for a relevant characterization of solar cell transport losses, and (iii) how the dependence of ρ_c to a change in the injected carrier density within the c-Si bulk provides additional insight to compare the illumination responses of different SHJ n-type contact stacks. To complete our experimental results, technology computer-aided design (TCAD) simulations are used to model the TLM structure and to identify the physical phenomena and the key parameters affecting ρ_c and the selectivity of several SHJ n-type contact stacks. In addition, the suspected limitations and physical phenomena appearing during such TLM measurements are elucidated. Overall, this work provides additional important insights into the fundamental understanding and the practical characterization of SHJ solar cells, as well as useful methods to guide the actual efficiency improvement of such devices toward their practical efficiency limits.

II. METHOD

A. Shell of solar cells

1. General frame

In an approach proposed by Cuevas *et al.*,¹ a solar cell can be seen as a balloon inflated with light-generated carriers. This “balloon” corresponds to the solar cell absorber where electron-hole pairs are generated by converting the energy of the incoming light. In general, to efficiently extract these photo-generated carriers out of the absorber bulk, three electrical functions must be fulfilled, namely, (i) passivation, to avoid recombination at the surface of the absorber, (ii) selectivity, to spatially separate the holes and the electrons at different absorber locations, and (iii) terminal electrodes to extract the carriers outside the absorber and to inject them into an external load. Previously, the term *membrane* was introduced by Würfel⁸ to describe materials providing selectivity, and similarly the term *skin* was proposed by Cuevas *et al.*^{1,9} to describe passivation in addition to selectivity. Recently, following the pioneering work of Yablonovitch,¹⁰ the ability to provide selectivity in addition to passivation has been defined as a *carrier-selective passivating contact* (CSPC), i.e., a contact that passivates the surface of the absorber and that blocks one type of carriers to

escape from the absorber, while allowing the other one to be extracted. Prime examples of CSPC are the SHJ technology,⁷ as well as various approaches based on a thin tunneling oxide capped with polycrystalline silicon, such as the TOPCon¹¹ and the POLO¹² concepts. However, in these cases, the term *contact* is ambiguous, as it can equally refer to many different sub-elements constituting it.¹³ Indeed, all so-called *contact* schemes for solar cells actually consist of several stacked materials and/or material with locally changing properties, thus creating various interfaces and *contacts* between those. This section, therefore, aims at providing a generalized and unambiguous description of contacts in solar cells, allowing to accurately investigate—and eventually mitigate—the electrical and the optical losses affecting state-of-the-art solar cells: the terminology of *shell*.⁶

As defined in the frame of this work, the shell must fulfill the three above-mentioned electrical functions required for efficient carrier extraction, i.e., passivation, selectivity, and providing terminal electrodes. In addition, the shell must comply with optical requirements so as not to hinder the light absorption in the absorber. More specifically, at the front side of solar cells, the shell must be highly transparent to minimize the parasitic absorption losses. At the rear side, depending on the solar cell architecture, the shell might be required to be highly transparent as well (e.g., to ensure a high bifaciality) and to provide, in addition, a high internal reflection to increase the photons' optical path in the absorber bulk. As a result, the most important challenge of a shell is to fulfill all these electrical and optical functions altogether with as few losses as possible, to achieve high quality light collection and carrier extraction, thus eventually allowing high conversion efficiency. Depending on the solar cell technology, the shell may consist of a unique material with locally changing properties and/or of a stack of several thin layers made from different materials. The doping gradient in the silicon absorber used in the Al-BSF technology is a typical example of the former case, whereas the intrinsic and doped hydrogenated amorphous silicon, transparent conductive oxide (TCO), and metal layer stacks in the SHJ technology are perfect examples of the latter. Generalizing, it means that the shell includes all the parts of the solar cell located at both sides of the absorber between the near-surface modified region of this latter to the last terminal electrodes included before the external load. Importantly, the global shell characteristics and its ability to provide the three required electrical functions, as well as the optical ones, are defined by the global coupling of all of the components constituting it. In the case of electrical properties, this coupling is evidenced by the energy band bending occurring when the different elements constituting the shell are brought together. Note that because of this coupling, the “influence” of the shell might also extend into a part of the absorber bulk close to its surface, such as a space charge region (SCR) induced via the energy band bending. This is depicted in Figs. 1(a) and 1(b).

As briefly mentioned above, in the specific case of the SHJ technology, the shell is composed of a stack of several thin layers made out of different materials. These are intrinsic hydrogenated amorphous silicon [a-Si:H(i)], doped hydrogenated silicon layers, TCO, and metal layers, deposited on both sides of the n-type silicon bulk [c-Si(n)]. Such a shell in the case of a two side-contacted solar cell is illustrated in Fig. 1(a) (note that in back-contacted solar cells, the purposes of the front of the shell are

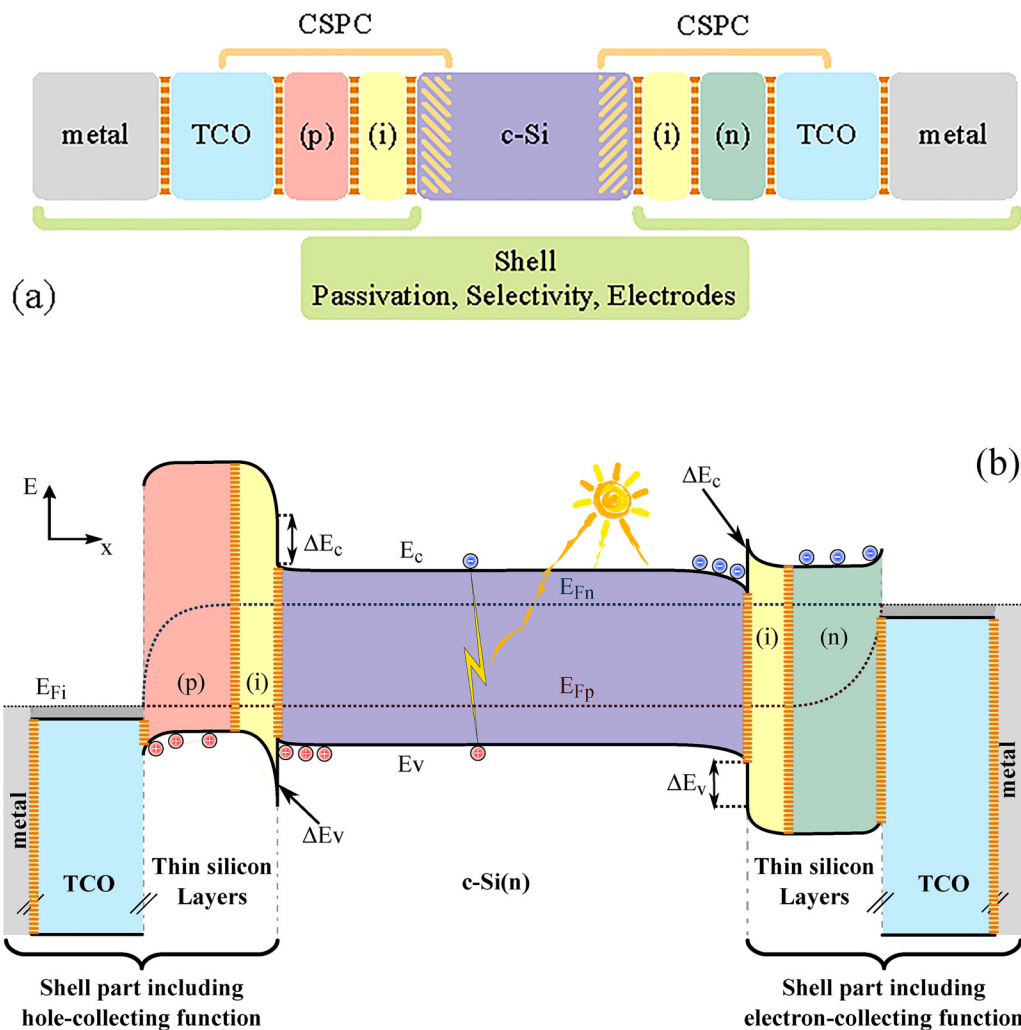


FIG. 1. (a) Sketch of an SHJ shell in the case of a typical two side-contacted solar cell. The c-Si bulk, coupled with the two parts of the shell (encompassing the different material layers), is represented. These are the intrinsic amorphous layer (i), p and n-type thin silicon layers [(p) and (n), respectively], as well as TCO and metal layers. All these sub-layers coupled together define the three different electrical functions (passivation, selectivity, and terminal electrode) that are partly revealed in the energy-band diagram in (b). The several interfaces and sub-contacts defined by the different sub-layers are represented in orange-hatched areas. Finally, the CSPEC range effect extending from the TCO to inside the c-Si bulk is also represented in light-orange dashed areas. (b) Corresponding schematic energy-band diagram in the space domain for open-circuit condition and under injection. The conduction and the valence band energies (E_c and E_v , respectively), as well as the band bending (spatial evolution of the energy states), are represented spatially for the different SHJ material layers. The electron and hole quasi-Fermi levels (E_{Fn} and E_{Fp} , respectively) are also depicted spatially through the c-Si(n) bulk and the shell. The conduction and the valence band offsets with their respective energies (ΔE_c and ΔE_v , respectively) are also depicted. The latter build different energy barriers affecting the transport of the generated carriers.

passivation and optical losses minimization only, since the carrier-selective and electrode aspects are performed by the rear of the shell in addition to passivation). In this case, it appears clearly that the shell is composed of several interfaces and sub-contacts defined by the coupling of the different thin layers and the silicon bulk. The latter are highlighted as orange-hatched areas in Figs. 1(a) and 1(b). The coupling of the physical properties of the different materials, including the c-Si(n) bulk, defines the overall energy band bending presented in the space domain in

Fig. 1(b) and shapes the global electrical properties. Thus, because of this coupling, the addition, removal, or change of a single shell sub-component or of the c-Si(n) bulk directly affects the global energy-band arrangement, the latter being difficult to predict precisely *a priori*. Each shell layer must then be developed considering its resulting coupling with all other sub-components and the silicon bulk. It is, thus, challenging to optimize only one part of the SHJ shell without affecting the resulting electrical properties. Closing this comprehension gap requires taking a closer look at

the way the photo-generated carriers move within the energy-band structure; this is the topic of Sec. II A 2 below.

2. Carrier transport, contact resistivity, and selectivity

Transport is defined in this work as every single displacement of photo-generated carriers, expressed by the change in carrier concentration along position and time (continuity equation), from their generation location until their extraction at the terminal electrodes of the shell. The transport is, thus, the flow of both carrier types from the absorber through the shell, in their way to their selective areas and final respective electrodes. The quality of the carrier transport is impacted by two physical phenomena, namely, recombination and resistive effects, both resulting in electrical losses. Recombination is the result of a loss of carriers that induces a chemical potential drop; its magnitude is defined by the absorber bulk quality and the shell passivation ability. In contrast, resistive effects are the result of drift diffusion and interface's phenomena that induce an electrical potential drop when both carrier types flow from their generation location inside the absorber to the terminal electrodes, passing through the shell. Both electrical losses impact the final device performances, with the pseudo voltage (pV) reflecting the recombination losses and the series resistance (R_s) reflecting the resistive losses.^{1,8} To achieve a high fill factor (FF), and eventually high conversion efficiency, pV must be maximized, while R_s must be minimized. Nowadays, in state-of-the-art, single junction, crystalline silicon (c-Si) based solar cells, the contribution of the c-Si bulk to the remaining electrical losses no longer limits the solar cell performances, as it operates close to its Auger limit and features a suitable conductivity.¹⁴ Rather, the main contributions to the remaining electrical losses are dictated by the shell itself; therefore, best-in-class c-Si solar cells are nowadays *shell-limited* devices.^{15,16} It turns out from this electrical transport analysis that improving the conversion efficiency of c-Si solar cells requires a mitigation of the recombination losses and the resistive effects incurred by the shell. To do so, the shell must facilitate a large quasi-Fermi-level splitting inside the bulk in addition to a minimal chemical drop until the terminal electrodes, together with providing minimal supplemental resistive effects besides the absorber's own resistance.

As already mentioned in Sec. II A 1, SHJ shells aim at meeting these requirements by combining thin layers of different materials. However, this layer combination induces several energy barriers stemming from discontinuities in the energy-band structure, arising at the hetero-interfaces created between the different materials constituting the SHJ shell, leading to resistive losses.¹⁷ Such energy barriers are clearly visible in the energy-band diagram of the SHJ shell sketched in Fig. 1(b), e.g., at the interface between the c-Si(n) bulk and the intrinsic amorphous silicon layers as well as between the doped thin silicon layers and the TCO. The overall energy band bending and alignment, including the energy barrier characteristics (such as their height and width), is governed by the coupling of the physical properties of the different materials constituting the shell as well as by the c-Si(n) bulk properties. In particular, the band bending is defined by the Fermi energy within the device, from c-Si bulk to TCO. More precisely, the Fermi and quasi-Fermi levels are determined by the c-Si absorber carrier

density, the thickness, the activation energy (E_a), and the defect density of the thin silicon layers, as well as the work function (WF) and the carrier concentration (N_{TCO}) of the TCO layer, among others.^{4,18} These physical parameters define the energy position of the conduction and the valence bands with respect to the Fermi level for the c-Si wafer and for each material layer. Carrier transport through the hetero-interfaces located along the energy-band diagram occurs by two different general mechanisms, namely, thermionic emission and tunneling. In the specific case of SHJ shells, several tunneling processes have been identified¹⁹ and thoroughly described, these are: direct tunneling (DT),²⁰ band-to-band tunneling (B2BT),²¹ and trap-assisted tunneling (TAT).²² These processes are, thus, connected to the band bending at the c-Si/a-Si:H(i), a-Si:H(i)/doped thin silicon layer and doped thin silicon layer/TCO interfaces. Eventually, when all these effects result in an ohmic current-voltage (I-V) behavior under relevant operating conditions, the corresponding resistive electrical transport losses affecting carrier extraction can be accounted by a contact resistivity value (ρ_c). In that case, this parameter allows one to assess the global carrier transport quality through all the hetero-interfaces and the materials constituting SHJ shells. Any change to the energy barriers or to the bulk properties of the materials constituting the shell and of the c-Si bulk will directly affect the ρ_c value.¹⁷ The parameter ρ_c then reflects the effect of the global band bending on transport resulting from the property coupling of the different materials and is, therefore, a relevant parameter to investigate different interfaces within and induced by the shell.

More specifically, at the vicinity of the c-Si/a-Si:H(i) interface, a change of the c-Si bulk injected carrier density, i.e., a quasi-Fermi-level change inside the c-Si bulk, will affect the local band bending inside the c-Si bulk and, thus, affect the accumulation of carriers at this location, potentially impacting the ρ_c value. Said differently, the value of ρ_c is expected to depend strongly on the injection conditions. On the other hand, the energy band bending also rules the selectivity of a given shell. Indeed, in the case of SHJ, selectivity is ruled by the ratio between the conductivities of majority and minority charge carriers inside the absorber at the vicinity of the c-Si/a-Si:H(i) interface.⁵ Yet, as electron and hole mobilities are of the same order of magnitude inside c-Si,^{23,24} a high selectivity requires a high asymmetry in carrier concentration close to this interface. In the case of SHJ, this asymmetry results in carrier accumulation inside the c-Si bulk close to the c-Si/a-Si:H(i) interface, such as the higher the accumulation the higher the selectivity.^{25,26} To enforce different accumulation conditions, the activation energy of the thin silicon layers was proven to be a relevant parameter. This parameter is equal to the energy difference between the Fermi level and the current transporting band, i.e., the conduction band for the case of electrons and the valence band for the case of holes. Thus, the lower the E_a , the higher the doping of the thin silicon layer. As demonstrated in Ref. 4 a low (respectively high) E_a was found to allow for a high (respectively low) selectivity owing to a high (respectively low) accumulation close to the c-Si/a-Si:H(i) interface. Consequently, for SHJ shells, ρ_c and selectivity are expected to depend on the injection condition, for instance induced by variable illumination: this forms the rationale of our investigation.

B. TLM sample fabrication and measurement

TLM samples were fabricated on 240- μm -thick, float-zone n-type c-Si wafers [c-Si(n)] with a resistivity of $2.8\ \Omega \cdot \text{cm}$. The wafers were textured on both sides in an alkaline solution to create random pyramids and then wet chemically cleaned. Before the deposition of the required layers, the native silicon oxide was removed in a diluted hydrofluoric solution. Then, a thin blanket of a-Si:H(i) films were deposited on both sides of the wafer for surface passivation by plasma-enhanced chemical vapor deposition (PECVD), using an Indeotec Octopus II system. Then, a thin blanket p-type a-Si:H film [a-Si:H(p)] was immediately deposited, with the same deposition system, at the rear of the TLM samples. On the front of the TLM samples, different n-type thin silicon multilayers combining a thin bottom amorphous buffer layer and different top nanocrystalline layers [referred to as a-Si:H(n)/nc-Si:H(n)] were deposited to reach different E_a (see Table I). The thin bottom buffer a-Si:H(n) layer was kept the same for all multilayers. More details on our thin silicon layer stacks can be found elsewhere.^{27–30} Afterward, an indium tin oxide (ITO) layer was deposited at the rear of the TLM samples, on the top of the a-Si:H(p) layer, using DC magnetron sputtering with an $\text{In}_2\text{O}_3\text{:SnO}_2$ (ITO) target. The thickness of this rear ITO layer measured on a planar bare glass substrate was 110 nm, which led to an optimal thickness for anti-reflective coating (ARC) on textured wafer. The combination of a-Si:H(i)/a-Si:H(p)/ITO at the rear of the TLM samples then allows to achieve a good passivation quality, together with an optimized ARC, and, thus, to maximize the injected carrier concentration reached in the c-Si(n) bulk of the TLM samples for a given illumination. Note that the presence of the a-Si:H(p) layer prevents any electron current to pass through the ITO rear layer, hence restricting it to the c-Si(n) bulk. At the front of the TLM samples, aluminum-doped zinc oxide (AZO) was deposited by RF magnetron sputtering with an Oerlikon Clusterline tool on the different n-type thin silicon multilayers. This AZO layer features a carrier concentration of $1.5 \times 10^{20}\text{ cm}^{-3}$ and a thickness of 180 nm on a glass substrate. The different shells manufactured, as presented above and used for this study, are listed in Table I. Shells 1 to 4 feature similar high passivation quality at the rear but different n-type multilayers at the front with thickness ranging from 34 to 89 nm along with E_a from 17 to 265 meV. Shell 5 features the same n-type multilayers than shell 1 but a low rear passivation quality.

TABLE I. List of the different shells under study with the thickness and activation energy of a-Si:H(n)/nc-Si:H(n) as well as the quality of the rear passivation. The rear passivation quality is tuned with the a-Si:H(i)/a-Si:H(p) stack. The back ITO, the front AZO, and Ag are the same for all shells.

Shell	n-type multilayer		Rear passivation quality
	E_a (meV)	Thickness (nm)	
1	265	39	High
2	173	34	High
3	48	37	High
4	17	89	High
5	173	34	Low

The thicknesses of the n-type multilayers were measured on planar glass substrates using reactive ion etching to create a thickness step, its height being measured using a stylus profilometer. Their activation energy was determined by conducting a temperature-dependent dark conductivity measurement.³¹ The TCO thicknesses were assessed by using a stylus profilometer and their carrier concentration (N_{TCO}) was determined by performing the Hall effect measurement in the Van der Pauw configuration,³² in both cases on bare planar glass witness samples. Finally, a 400-nm-thick silver (Ag) rear blanket layer was sputtered over the whole AZO layer. After this step, the TLM samples were annealed at 210 °C for 30 min. It is important to note that, thanks to our large-area PECVD and PVD tools, within a single experiment, all TLM samples were co-deposited with identical a-Si:H(i), a-Si:H(p), ITO, and rear blanket Ag layers. Therefore, only each specific n-type thin silicon multilayer and AZO deposition was performed individually for each TLM sample. Then, TLM patterns featuring a length (L) of 2 mm and gaps of 0.5, 1.0, 1.5, 2.0, 2.5, and 3.0 mm were printed using a protective ink mask. The Ag and AZO layers were then etched between the pads, and the ink was removed. After these etching steps, the TLM samples were cut with a selected width (w) of 6 mm to create edge isolation. This isolation is needed to confine the current flow and to avoid additional errors caused by edge effects, i.e., to prevent the current flowing away from the edges of the TLM pads before being recollected. To do this, the TLM samples were first pre-cleaved at the rear using a laser and then cut manually. Then, the interpad distances were precisely measured, thanks to a microscope, as they may slightly differ from their nominal value. A sketch of our typical TLM sample and design is given in Fig. 2. I-V measurements were performed on each completed TLM sample under dark conditions and under different illuminations using a Wacom class AAA light simulator and different filters to achieve an injected electron density (Δn_e) up to about $5.96 \times 10^{15}\text{ cm}^{-3}$, defining the 100% illumination level. The

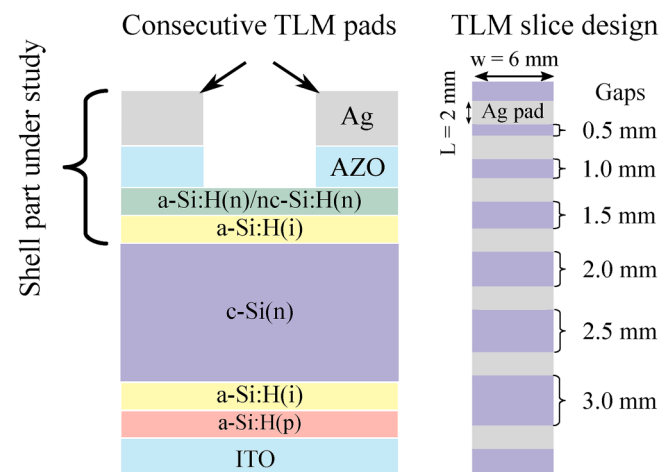


FIG. 2. Cross section of the experimental samples (left) and top view showing the TLM pad layout (right).

TLM samples were illuminated from the a-Si:H(i)/a-Si:H(p)/ITO side using a flip table to ensure a homogeneous injection below and between each TLM pad. From these I–V curves, the TLM computation was performed, and the output parameters, namely, the contact resistivity (ρ_c), contact resistance (R_c), sheet resistance (R_{sh}), and transfer length (L_T), were extracted. Finally, corrections on the value of ρ_c considering the wafer thickness of the TLM samples were performed for each illumination, as presented in Ref. 33. Finally, for each illumination, the ΔN_e values were calculated from the wafer R_{sh} , taking into account the dependence of the electron mobility on the injection.²³

C. Finite element simulations for TLM

To model the TLM structure and to simulate the value of ρ_c as a function of the c-Si(n) bulk injected carrier density, optoelectrical simulations were performed using TCAD Sentaurus.³⁴ This simulation platform rigorously solves the drift-diffusion equations together with interface physics (tunneling, thermionic emission, recombination, etc.). This allows to consistently assess the transport mechanisms through the hetero-interfaces of the shells under study. The simulated TLM structure consists of two identical contact pads on top of a c-Si(n) bulk spaced by variable gaps as used on the actual sample (0.5, 1.0, 1.5, 2.0, 2.5, and 3.0 mm). Each contact width is 1.0 mm, and the n-type contact stack is formed by 6 nm of a-Si:H(i), 30 nm of an n-type thin silicon layer, and 180 nm of TCO. The c-Si(n) bulk features a wafer resistivity of $3\ \Omega\text{ cm}$, which gives a doping of $1.55 \times 10^{15}\text{ cm}^{-3}$. The E_a values were adjusted by a uniform doping concentration in a defective background of doped layers to achieve 17, 48, 173, and 265 meV (similar to the experimental values presented in Table I). The TCO was modeled as a degenerate semiconductor;^{4,35} thus, work-function mismatches and induced band bending are accurately considered. The TCO carrier concentration (N_{TCO}) was set to $1.44 \times 10^{20}\text{ cm}^{-3}$. Further details on the TLM modeling can be found in Refs. 4, 17, and 36. To change the injected carrier density inside the c-Si bulk for a given shell, different injection levels, and, thus, different electron quasi-Fermi levels (E_{Fn}), are emulated inside the c-Si bulk absorber using different carrier generation rates equivalent to the targeted light intensities. A reference optical generation profile was adjusted based on ray-tracing optical simulations to reach 39 mA/cm^2 , which is a typical current density in solar cells using SHJ shells. This generation profile was fixed to be the 100% of illumination, and accordingly, TLM structures were evaluated in the dark with 7, 13, 50, and 100% illumination by scaling the generation rate. The recombination rate inside the c-Si bulk (τ_{bulk}) was adjusted to reach a ΔN_e of about $4.85 \times 10^{15}\text{ cm}^{-3}$ for the 100% illumination. The corresponding energy-band diagrams for these different illuminations were simulated and considered. From the latter, the SCR widths (w_{SCR}) inside the c-Si(n) bulk were calculated considering its extent from the first decreasing point of the energy conduction band (E_c) to the c-Si(n)/a-Si:H(i) interface location. The conduction band energy height (E_h) was also calculated considering the energy difference between the flat part of E_c and the minimum energy at the c-Si(n)/a-Si:H(i) interface. Finally, the electron and hole accumulations were calculated by determining the ratio of the electron (respectively, hole)

density at the c-Si(n)/a-Si:H(i) interface to the electron (respectively, hole) density inside the bulk. These parameters were calculated for the different illuminations and E_a under study. Then, each TLM structure was simulated to obtain the current $v.$ voltage response from -1 to 1 V, and the TLM methodology was applied to extract R_{sh} and ρ_c .

D. Edge recombination impact on contact resistivity measurement

As described in Sec. II A 2, the TLM samples under investigation have cut edges to create current isolation. Their edges are consequently unpassivated and important recombination losses occur there. Under illumination, this induces a non-homogeneous excess carrier concentration from the middle of the TLM pad width (w) to its edges, thus leading to a corresponding c-Si(n) wafer resistivity variation. The latter is expected to be lower at the center of the pads than at the edges. Consequently, R_{sh} of the c-Si(n) TLM conductive layer is non-homogeneous and varies along the w direction. This again breaks one of the fundamental hypotheses of TLM that assumes homogeneous R_{sh} to ensure an evenly distributed current flow between two pads. *A priori*, there is no simple way to rigorously extract the contact resistivity in such a case. However, it is possible to evaluate its impact on the ρ_c value extracted with the standard TLM approach. To do this, the one-dimensional drift-diffusion solver PC1D³⁷ is used to simulate an inhomogeneous excess carrier concentration profile inside a 1D structure, allowing to consider one direction corresponding to the direction parallel to w in real samples. The material of the 1D structure is defined as a c-Si(n) bulk with a doping of $1.7 \times 10^{15}\text{ cm}^{-3}$, which is close to the value measured on experimental samples. Its length is set to 6 mm corresponding to the width of the actual TLM samples. The interface recombination velocities for electron (S_n) and holes (S_p) at both edges are assumed to be equal to $S_n = S_p = 10^7\text{ cm/s}$, which corresponds to the highest thermal velocity of carrier transport and is large enough to consider that all excess carriers have recombined at the edges. The simulated 1D structure used is depicted in Fig. 3 and compared with an actual TLM sample. To simulate the different illuminations under study, several generation profiles are defined. Each of them is established to be homogeneous for each position inside the simulated structure in order to reproduce the experimental generation of the TLM sample. The latter being illuminated from the back, the generation is then homogeneous along the w direction. The 1 sun generation profile is set to an average constant generation of $9.68 \times 10^{18}\text{ cm}^{-3}\text{ s}^{-1}$. This generation corresponds to the typical value present inside SHJ solar cells using similar thin silicon layers, TCO, and bulk thickness as the actual TLM samples. Finally, the carrier lifetimes defined experimentally by bulk and shell passivation quality are simulated in PC1D using the single Shockley–Read–Hall lifetime parameters (τ_{SRH}). Thus, by solving the drift-diffusion equation for this 1D test structure with PC1D, it is possible to simulate the electron density profile ($N_e(x)$) along the 1D direction. This profile is expected to be representative of what can be observed in an experimental TLM structure, along the pad width direction, assuming negligible transport in the other directions. Thus, considering a TLM c-Si(n) bulk of thickness d , it is possible to calculate the corresponding electron sheet resistance profile $[R_{sh}(x)]$ for any x_i position below the TLM pad using

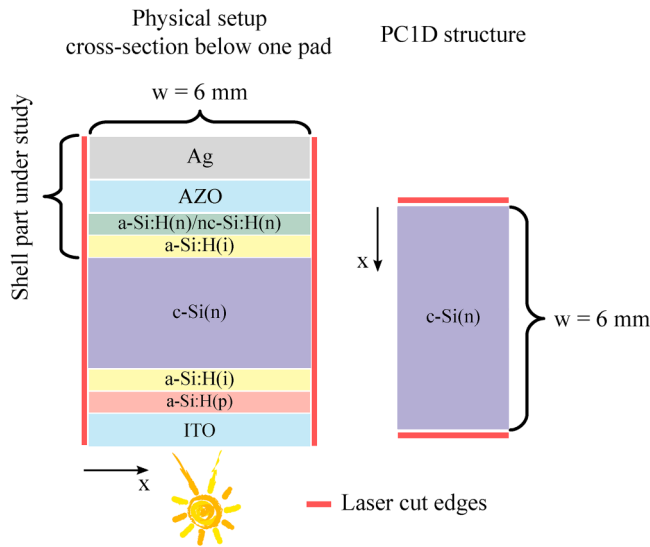


FIG. 3. Schematic description of the PC1D structure for simulating the recombination effects at the TLM sample edges.

Eqs. (1) and (2), with q being equal to the elementary charge and an electron mobility (μ_n) of $1330 \text{ cm}^2 \text{ V}^{-1} \text{ s}^{-1}$, assuming that in the range under study, the photogenerated carriers have little impact on mobility,^{23,24}

$$\sigma_e(x_i) = q\mu_n N_e(x_i), \quad (1)$$

$$R_{sh}(x_i) = \frac{1}{\sigma_e(x_i) \times d}. \quad (2)$$

Here, x_i stands for the i th position of the simulation domain mesh. From the $R_{sh}(x)$ profiles, it is then possible to calculate an average value of equivalent R_{sh} ($R_{sh_{eq}}$) with Eq. (3), which is approximated by considering the conduction of parallel resistances between two TLM pads. This approach, thus, ignores the lateral transport effects in the wafer along the TLM width direction, as was done in Ref. 38 for evaluating the impact of silver line resistance on TLM structures, where it was shown to have very little impact,

$$R_{sh_{eq}} = \frac{1}{\sum \left(\frac{\Delta x_i}{R_{sh}(x_i)} \right)} \times \sum x_i. \quad (3)$$

Under injection, $R_{sh}(x)$ is experimentally driven by the bulk and surface recombination of the actual TLM samples. In the simulation, all recombinations are lumped in one τ_{SRH} term, which is then adjusted to get $R_{sh_{eq}}$ simulated from PC1D to match the average value of R_{sh} measured experimentally for each illumination. Then, in the case of a ρ_c that depends on the excess carrier concentration, as it is the case in this work and will be presented in Secs. III A 2 and III C, a contact resistivity profile ($\rho_c(x)$) induced

by $R_{sh}(x)$ is present below the TLM pad width. From $\rho_c(x)$, it is possible to calculate the transfer length profile ($L_T(x)$) and contact resistance profile ($R_c(x)$) present below a pad using the TLM equations [Eqs. (4) and (5)] with $L = 2 \text{ mm}$ being the TLM pad length,

$$L_T(x_i) = \sqrt{\frac{\rho_c(x_i)}{R_{sh}(x_i)}}, \quad (4)$$

$$R_c(x_i) = \frac{\rho_c(x_i)}{\Delta x_i L_T(x_i)} \times \coth\left(\frac{L}{L_T(x_i)}\right). \quad (5)$$

Then, knowing R_c and R_{sh} for all positions x_i on the x mesh, and considering all the resistance in parallel (i.e., ignoring here again lateral transport along the TLM width direction), it is possible to compute the total TLM resistance (R_{TLMk}) for each interpad distance k using Eqs. (6) and (7),

$$\frac{1}{R_{TLMk}(x_i)} = \frac{1}{2R_c(x_i) + R_{sh}(x_i) \times \frac{gap_k}{\Delta x_i}}, \quad (6)$$

$$R_{TLMk} = \frac{1}{\sum \left(\frac{1}{R_{TLMk}(x_i)} \right)}. \quad (7)$$

Finally, from the plot of R_{TLMk} as a function of the interpad distance, k , it is possible to perform TLM computation and to get the values of $R_{sh_{eq}}$, R_c , L_T , and, thus, ρ_c . These output parameters that are obtained by considering an inhomogeneous $R_{sh}(x)$ profile are then compared with the ones obtained experimentally using the standard TLM computation that consider homogeneous R_{sh} , i.e., ignoring the R_{sh} inhomogeneity due to edge recombination.

III. RESULTS AND DISCUSSION

A. Finite element simulations for TLM measurements

1. Illumination and non-ohmic behavior

During our investigation, one of the first observed phenomena was the presence of non-ohmic TLM I-V curves with the augmentation of the illumination. This phenomenon was thoroughly investigated as it was first thought to be a limitation to perform TLM computation. Indeed, a non-ohmic behavior will break the fundamental TLM hypothesis requesting the ohmicity of the shell part under investigation. Figure 4(a) shows the simulated I-V curves obtained between two TLM pads as a function of the illumination for a shell with τ_{bulk} of 0.4 ms . It is observed that a non-ohmic behavior appears above a certain illumination threshold, here 13%. This non-ohmic behavior becomes stronger as the illumination increases and is independent of the different E_a under study (data not provided). Additionally, Fig. 4(b) plots the simulated I-V curves between two TLM pads under 13% illumination for different τ_{bulk} . In this case, it is observed that the non-ohmic behavior becomes increasingly noticeable upon the rise of τ_{bulk} , again regardless of the E_a value (data not given). In both cases presented in Figs. 4(a) and 4(b), increasing the illumination or the τ_{bulk}

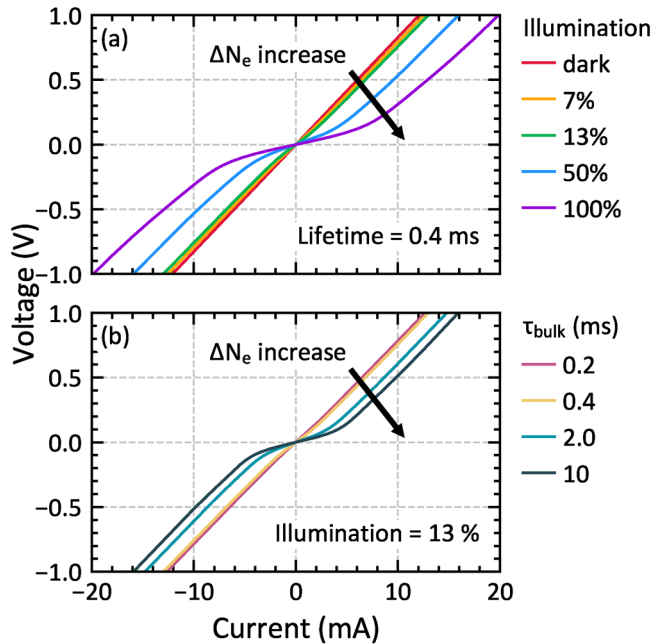


FIG. 4. Simulated I-V curves between two TLM pads as a function of the illumination for a τ_{bulk} fixed to 0.4 ms (a) and as a function of the bulk lifetime for an illumination fixed to 13% (b).

results in an augmentation of the generated carrier concentration inside the c-Si bulk. Thus, the trigger of the non-ohmic behavior is revealed to be the quantity of injected carriers inside the c-Si(n) bulk, rather than the illumination level or the recombination mechanisms alone. This non-ohmic behavior is, therefore, proven not to stem from an effect of the shell properties but from the c-Si bulk properties. The experimental pieces of evidence, as well as the physical origin of the non-ohmic behavior and how to accurately extract the value of ρ_c in these conditions, are presented in Secs. III B 1 and III B 2.

2. Illumination and impact on ρ_c

Figures 5–8 show the impact of changing E_a of the n-type thin silicon layer (17, 48, 173, and 265 meV) and of varying the illumination on the following: the conduction band energy in the space domain (Fig. 5), the two band parameters w_{SCR} and E_h (Fig. 6), the electron and hole accumulations (Fig. 7), and the ratio of electron to hole at the c-Si(n)/a-Si:H(i) interface (Fig. 8). On the one hand, it is observed that as expected, in the dark, the electron accumulation is more pronounced for a low E_a than for a high E_a . Upon increasing E_a from 17 meV to 265 meV, w_{SCR} decreases from 820 to 725 nm and E_h decreases from 0.22 to 0.13 eV (see Fig. 6), resulting in an electron accumulation reduction from 2.91×10^3 to 8.86×10^1 [see Fig. 7(a)]. On the other hand, the hole accumulation is found to be higher for a high E_a than for a low E_a , increasing from 3.25×10^{-4} to 1.13×10^{-2} [see Fig. 7(b)]. Finally, looking at the ratio of electron to hole at the c-Si(n)/a-Si:H(i) interface, it is

observed that the latter is higher for a lower E_a (see Fig. 8). Overall, this highlights that a higher electron accumulation and, thus, a higher electron selectivity in the dark is obtained for a lower E_a , as discussed in Secs. II A 2. Then, looking at the different illuminations, we observe that for all E_a considered here, the conduction band and the quasi-Fermi level are getting closer, resulting in an electron density augmentation (see Fig. 5) and affecting the band parameters: indeed, E_h and w_{SCR} decrease upon increasing the illumination (see Fig. 6). This will directly affect the electron accumulation that is found to reduce with the illumination increase [Fig. 7(a)]. In addition, by increasing the illumination, the hole density rises as well, impacting the hole accumulation that is found to increase upon illumination for all the different E_a under investigation [see Fig. 7(b)]. In particular, the ratio of electron to hole at the c-Si(n)/a-Si:H(i) interface reduces with the illumination increase, demonstrating that the electron selectivity is, therefore, impacted by illumination such as the higher the illumination, the lower the electron selectivity (Fig. 8). Overall, Figs. 5–7 show that the decrease in the value of these parameters is independent of E_a but is dependent only on the illumination. In addition, when the illumination varies, the electron (respectively, the hole) accumulation for a low E_a always stays higher (respectively, lower) than that for a high E_a .

Figures 9(a)–9(d) show the R_{sh} and ρ_c values extracted from TLM simulations for the different E_a and the various illuminations. Figure 9(a) shows that, as expected, the R_{sh} decreases with increasing the illumination; this behavior directly owes to an augmentation of the electron density (N_e) under higher illumination, the latter being the same for the four different E_a as the passivation quality is similar for the different shells under study. In contrast, Fig. 9(b) shows that ρ_c drastically increases with illumination for all the investigated E_a . It is observed that the higher the E_a , the higher the increase of ρ_c with illumination. Figure 9(c) shows ρ_c as a function of R_{sh} . Starting from the R_{sh} value in the dark (hence the bottom right points in the graph), it is observed that for all E_a , ρ_c increases linearly as the R_{sh} decreases, but with different slopes. These slopes correspond to the response of the n-type contact stacks to the illumination; said differently, the higher the slope, the higher the impact of the illumination and, thus, of the injected carrier density on the contact resistivity. The slopes extracted from the $\rho_c = f(R_{sh})$ linear curves are plotted in Fig. 9(d). Here, we observe that the higher the E_a , the higher the slope of the $\rho_c = f(R_{sh})$ curve and, thus, the higher the impact of the illumination on the shell under study. This may suggest that a higher electron accumulation, and, thus, a higher electron selectivity in the dark, will result in a lower slope and, thus, in a smaller impact of the illumination on the shell properties.

However, it is found that the absolute values of ρ_c are not directly related to the carrier accumulation variation upon illumination. Indeed, first of all, the variation of the electron and the hole accumulations in the dark with the rise of E_a is significant: from 2.91×10^3 to 8.86×10^1 for electrons and from 3.25×10^{-4} to 1.13×10^{-2} for holes, whereas the ρ_c variation remains relatively small, that is, from 1.06×10^{-2} to $1.63 \times 10^{-2} \Omega \text{ cm}^2$. Conversely, the electron and the hole accumulation variation with the illumination increase are significantly smaller: from 2.91×10^3 to 8.59×10^2 for electrons and from 3.25×10^{-4} to 9.61×10^{-4} for holes; however, in that case, the ρ_c variation is much larger, from 1.06×10^{-2} to $1.77 \times 10^{-1} \Omega \text{ cm}^2$ (for the case of shell 4 with

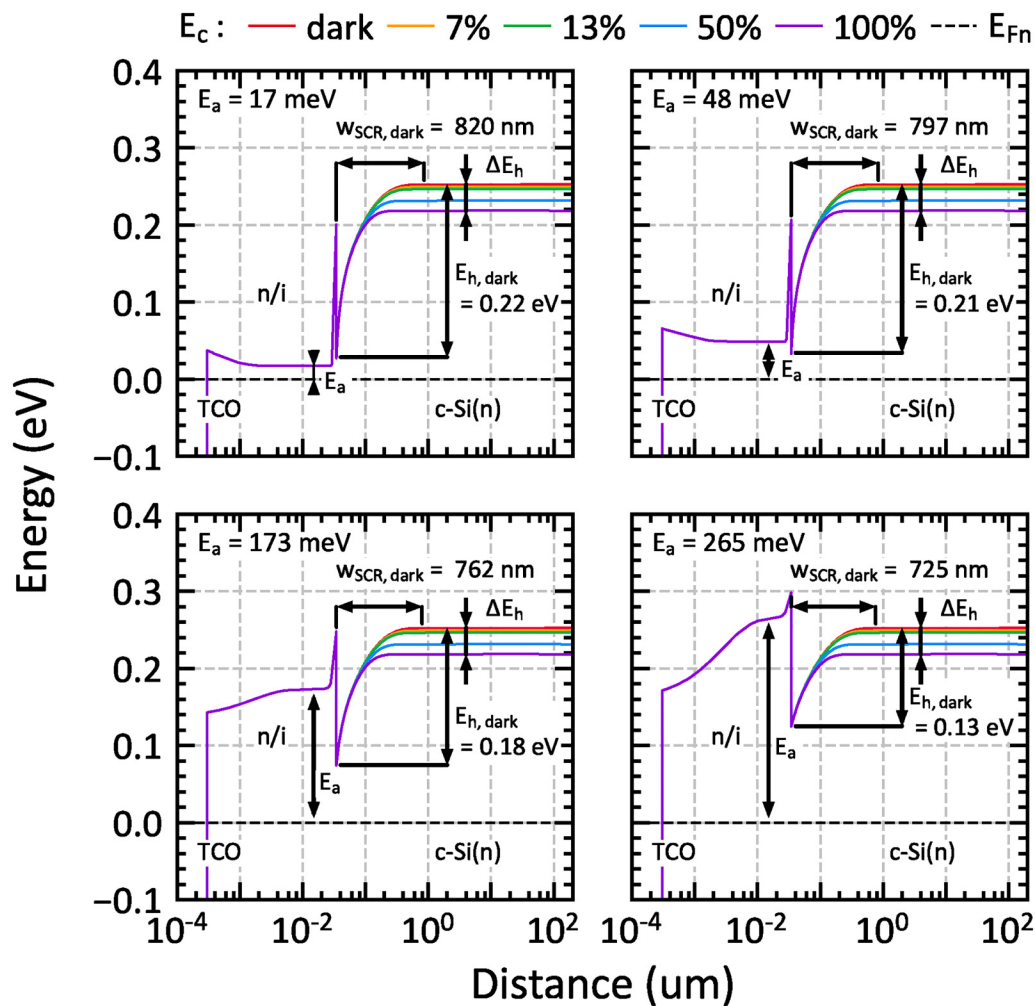


FIG. 5. Energy-band diagrams illustrating the different E_c as a function of the illumination for the different n-type thin silicon layers featuring E_a of 17, 48, 173, and 265 meV. w_{SCR} and E_h in the dark, as well as the difference of E_h between dark and 100% illumination (ΔE_h), are depicted.

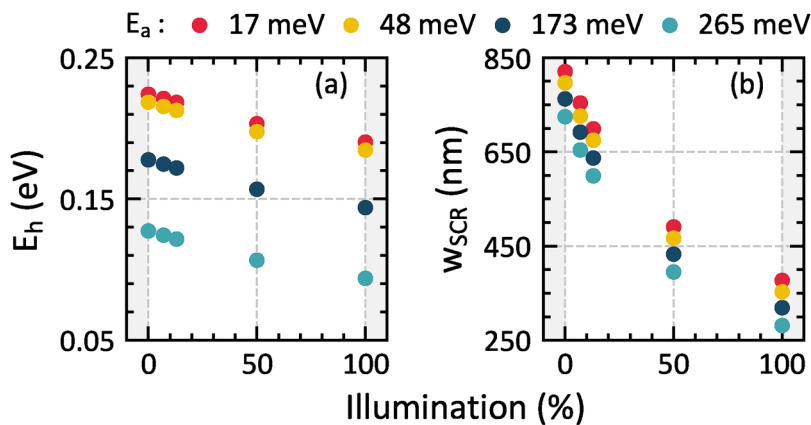


FIG. 6. E_h (a) and w_{SCR} (b) as a function of illumination for different E_a 's.

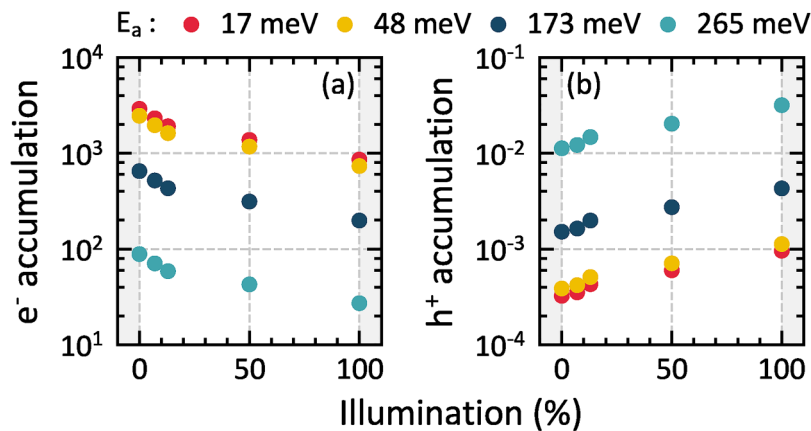


FIG. 7. Electron (a) and hole (b) accumulation as a function of illumination for different E_a 's.

$E_a = 17$ meV). In other words, as a prime example, the ρ_c value at 100% of illumination of shell 4 featuring an E_a of 17 meV is higher than the ρ_c value in the dark of shell 1 featuring an E_a of 265 meV, despite a higher electron and lower hole accumulation.

An additional outcome of these results is that considering a ΔN_e of about $2.0 \times 10^{15} \text{ cm}^{-3}$ at MPP³⁹ and, thus, an R_{sh} of about $50 \Omega/\text{sq}$, Fig. 9(c) shows that the difference between the ρ_c value calculated in the dark (corresponding to $R_{sh} \sim 110 \Omega/\text{sq}$) and at MPP is between 0.11 and $0.14 \Omega \cdot \text{cm}^2$ for the four different E_a . Hence, considering that a $1 \Omega \cdot \text{cm}^2$ R_s induces an FF loss of $\sim 5\%_{\text{abs}}$,⁴⁰ the difference between the induced FF loss calculated at MPP illumination and the one in the dark is between $0.57\%_{\text{abs}}$ and $0.70\%_{\text{abs}}$. It is, therefore, important to measure the ρ_c at MPP condition to study accurately the actual impact of a shell on the transport losses and, thus, on the corresponding effect on the FF of solar cells.

B. TLM under illumination and non-ohmic behavior

1. Experimental pieces of evidence

Figure 10(a) plots the I-V curves experimentally measured for shell 2, featuring an n-type multilayer with the E_a of 173 meV and

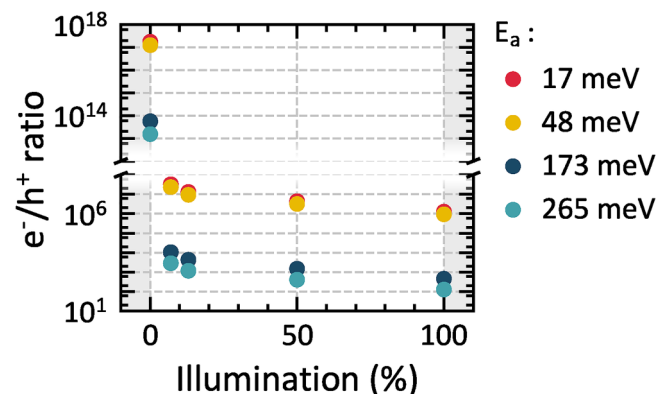


FIG. 8. Ratio of electron to hole at the c-Si(n)/a-Si(i) interface as a function of illumination for different E_a 's.

high rear passivation quality, under different illuminations and between two consecutive TLM pads spaced by 2.5 mm. The major observation here is the excellent agreement between the simulations presented in Sec. III A 1 and the experimental results: The non-ohmic behavior gets stronger with a higher illumination and, thus, with a higher ΔN_e . The ΔN_e corresponding to the different illumination conditions are given in Table II. Markedly, the non-ohmic behavior appears above a certain injected carrier density threshold, here, $2.2 \times 10^{15} \text{ cm}^{-3}$ for an illumination of 50%. In addition, as observed with simulation, the non-ohmic behavior is present for all of the shells under study with the high passivation quality (shells 1 to 4) listed in Table I. The latter appears at a similar illumination intensity threshold with similar ΔN_e values (data not provided), confirming that these shells feature similar passivation quality. Furthermore, the onset of the non-ohmic behavior is experimentally shown to depend on the passivation quality of the shell under study. This is illustrated in Fig. 10(b), which plots the TLM I-V curves under illumination of shell 5, featuring the same n-type multilayer as shell 2 (with, namely, E_a of 173 meV) but presenting a low rear passivation. Although the TLM I-V curves of shell 2 become non-ohmic with illumination increase, the ones of shell 5 stay ohmic for all illuminations. This is due to the different passivation qualities and hence to the different injected carrier densities actually reaching inside the c-Si(n) bulk for a given illumination. The injected electron density induced by the illumination for both shells is listed in Table II. Thus, it is experimentally validated that the injected electron density inside the c-Si(n) drives the non-ohmic behavior of the TLM samples, consistently with what was demonstrated by the numerical study presented in Sec. III A 1.

2. Simple explanation of the non-ohmicity

Here, the appearance of the non-ohmic regime is demonstrated to be due to a drift of the free carriers induced by the voltage applied between two consecutive TLM pads, leading to a non-homogeneous carrier density and, thus, to a variation of the wafer R_{sh} below the TLM pads and the gap in-between. Indeed, it is demonstrated by simulation and presented in Figs. 11(a) and 11(b) (top sketches) that for zero TLM bias ($\Delta U = 0 \text{ V}$), the generated carriers are homogeneously distributed inside the bulk [Fig. 11(a)], but

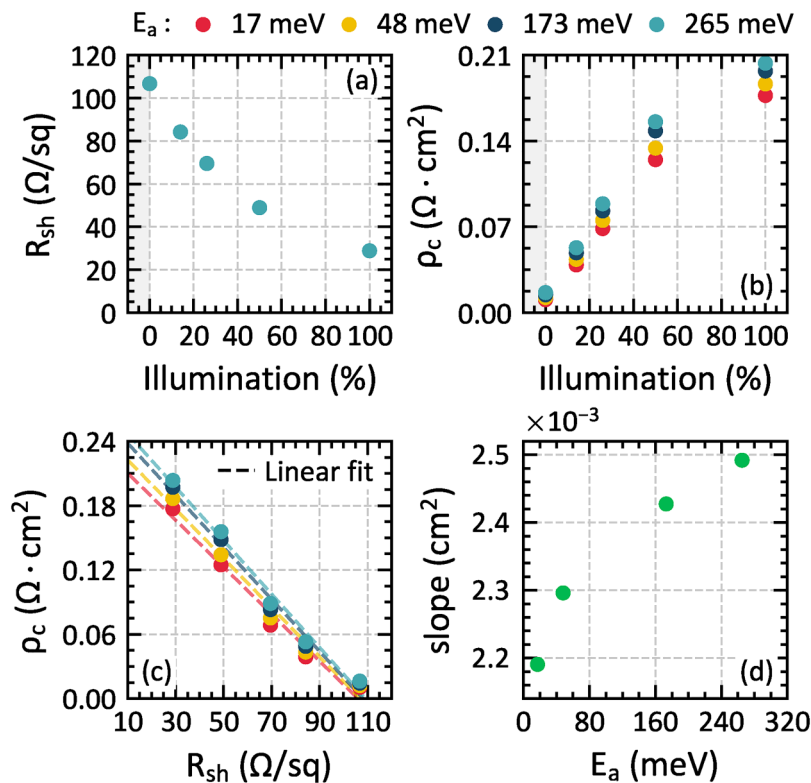


FIG. 9. (a) and (b) simulated R_{sh} and ρ_c as a function of the illumination intensity. (c) Simulated ρ_c as a function of R_{sh} and (d) slopes from simulated $\rho_c = f(R_{sh})$.

as soon as a non-zero TLM bias is applied, here simulated for one volt ($\Delta U = 1$ V), a drift of generated carriers arises, leading to an inhomogeneous carrier density inside the bulk and below both TLM pads [Fig. 11(b)]. A simplified case study to illustrate the impact of this effect is presented in Figs. 11(c) and 11(d) (bottom sketches). Under illumination and at $\Delta U = 0$ V (no TLM voltage bias), the electrons are homogeneously distributed inside the c-Si(n) bulk along

the distance L , and their density equals $n_{0e} + \Delta N_e$, with n_{0e} the bulk doping density, everywhere within the sample bulk. Under a TLM applied bias $\Delta U = \alpha V$ (with $\alpha > 0$), the electrons drift because of the applied external field. We now assume these electrons to be distributed following a simple non-homogeneous distribution: in the sample region $0 < x < L/2$, the electron density is now n_{0e} , whereas in the region $L/2 < x < L$, the electron density is $n_{0e} + 2\Delta N_e$. Note that

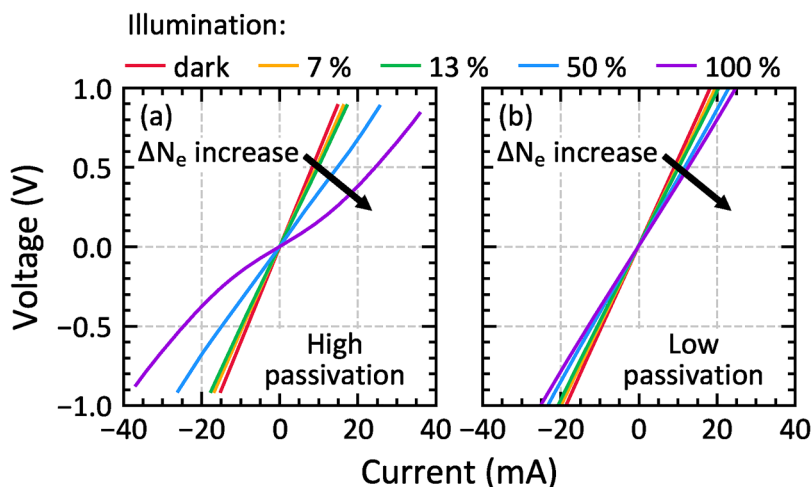


FIG. 10. I-V characteristics as a function of the illumination (in the case of a TLM gap of 2.5 mm) of shells 2 (a) and 5 (b), featuring both the same n-type multilayer with $E_a = 173$ meV, but with a high and a low rear passivation quality, respectively.

TABLE II. Injected electron density (ΔN_e) as a function of illumination for the high and low rear passivation quality of shells 2 and 5, respectively, both featuring an n-type multilayer with $E_a = 173$ meV.

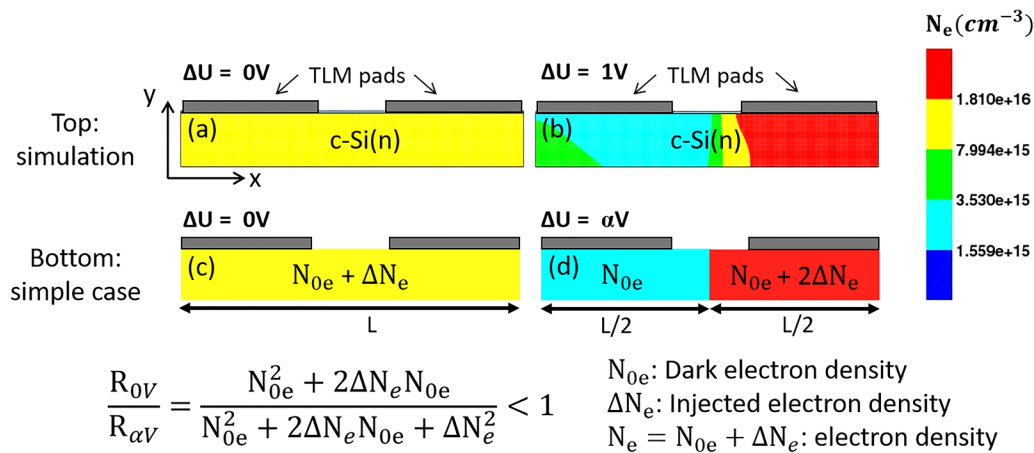
Illumination	ΔN_e (cm ⁻³) shell 2	ΔN_e (cm ⁻³) shell 5
Dark	0	0
7%	3.14×10^{14}	1.30×10^{14}
13%	4.85×10^{14}	2.22×10^{14}
50%	2.23×10^{15}	5.31×10^{14}
100%	6.55×10^{15}	7.84×10^{14}

the total number of electrons (and hence holes) is chosen to be constant inside the whole volume of the sample in both the 0 V and the α V cases. This is equivalent to assuming the same total recombination rate in both cases. Computing now the equivalent resistance of the sample bulk seen by the electrons in the 0 V and the α V cases (R_{0V} and $R_{\alpha V}$, respectively), it turns out that $R_{0V} < R_{\alpha V}$ (see the Appendix for the full calculation details). Said differently, the wafer resistance depends on the applied bias ΔU , i.e., $R = R(\Delta U)$. Hence, the higher the TLM applied bias, the higher the total resistance seen by the TLM current between two TLM pads (as $R_{\alpha V}$ gets consistently larger values than R_{0V}). This explains the non-ohmic shape of the I-V curve obtained between two TLM pads measured under illumination. At low voltages however, a linear I-V regime is still present, because the drift of charges is small, but as soon as the voltage rises, the non-ohmic I-V behavior appears and then stabilizes at high voltages to a second linear I-V regime. This stabilization is due to the presence of a maximal drift of carriers, such as the carriers are all completely depleted through the whole silicon bulk. In addition, this second linear regime features a higher slope (i.e., a higher resistance) than the first linear one, evidencing the increase of the c-Si global resistance with the voltage increase [see Fig. 10(a)]. Importantly, in any case where the TLM bias induced a

non-negligible drift of carriers, two different injection conditions are present below the two TLM pads, which then makes impossible to perform the TLM computation. Thus, to stay in a near-uniform injection throughout the wafer, we chose to perform the TLM computation taking the slope in the first linear regime of the I-V curves (symmetrically around the origin). Illustrative examples of such linear ranges are given in Fig. 12 in the case of shell 2. Note that this drift effect is expected to be present also for other test structures used for ρ_c characterization, such as the one presented in Ref. 41. In that case, the spatial variation in the excess carrier concentration will arise in the vertical direction and will also impact the resulting resistance of the c-Si bulk.

C. TLM under illumination and impact on ρ_c

Figures 13(a)–13(c) plot the TLM parameters obtained from our experimental measurements and for shells 1 to 4 featuring different E_a (17, 48, 173, and 265 meV, respectively). Figure 13(a) shows that, consistently with our simulations, the R_{sh} decreases with increasing the illumination for the different E_a . In addition, it is observed that for the different illuminations, the R_{sh} present similar values for each E_a , hence revealing similar passivation quality for the different shells under study. The injection conditions corresponding to the different illuminations are listed in Table III. Figure 13(b) shows that the ρ_c drastically increases with the illumination for the investigated E_a . In particular, it is observed that with the illumination, the distribution of ρ_c for the different E_a stays the same, but the difference in the value of ρ_c between the different E_a is more pronounced for a higher illumination. Figure 13(c) plots the ρ_c as a function of the R_{sh} experimentally obtained for the four different shells along with the linear $\rho_c = f(R_{sh})$ fitting curves. Remarkably, our experimental results are consistent with those obtained from numerical simulations (see Sec. III A 2). (Note that both experimental and simulation data follow the same trend when changing the illumination. However, by comparing the differences between the simulation

**FIG. 11.** Top: electron density for a 1 sun illuminated TLM sample, under 0 V (a) and 1 V (b) TLM voltage; Bottom: simplified case study with at 0 V (c) the total number of electrons homogeneously distributed inside the c-Si bulk along the distance L , and at α V (d), a particular non-homogeneous distribution. This simple case study illustrates that the higher the TLM applied bias, the higher the total resistance seen by the TLM current between two TLM pads ($R_{0V} < R_{\alpha V}$).

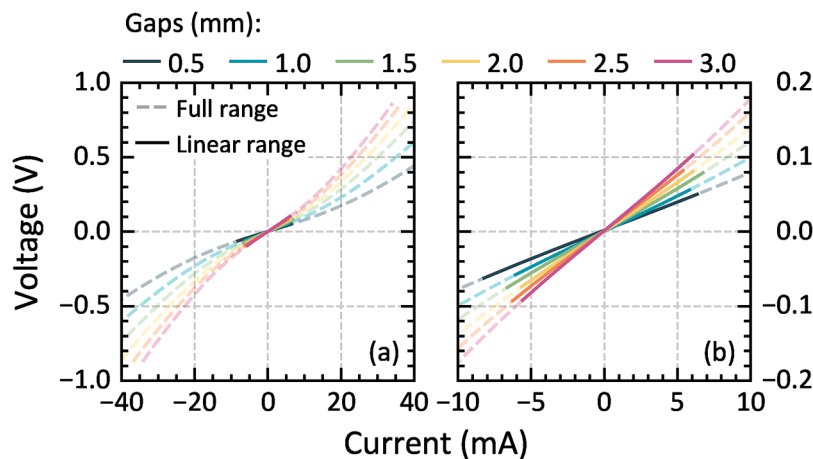


FIG. 12. I-V curves of shell 2 showing the linear ranges where TLM computation is performed for the case of 100% illumination and for the different gaps. (a) Full I-V range and (b) zoom on the linear range.

and the experimental results, it is observed that a much stronger impact of the activation energy on the ρ_c behavior is observed experimentally. This may be due to the fact that in the TCAD simulations, perfect hetero-interfaces at c-Si/a-Si:H and n-aSi:H/TCO are assumed. The discrepancies in contact resistivity magnitude between simulations and experiments are then likely suspected to come from the imperfect interfaces that are present in the experimental TLM samples). Indeed, the ρ_c value is found to increase linearly with the

R_{sh} decrease and the $\rho_c = f(R_{sh})$ fitting curves present different slopes for the different shells. The values of the slopes are presented in Fig. 13(d). Looking at the three E_a values of 17, 48, and 173 meV, it is observed that the higher the E_a , the higher the $\rho_c = f(R_{sh})$ curve slope as predicted by simulation. Generalizing the rationale explained in Secs. II A 2 and III A 2, we can, therefore, assume that the shell featuring E_a of 17 meV is the least sensitive to illumination, thanks to a high dark electron accumulation, and that the shell featuring E_a

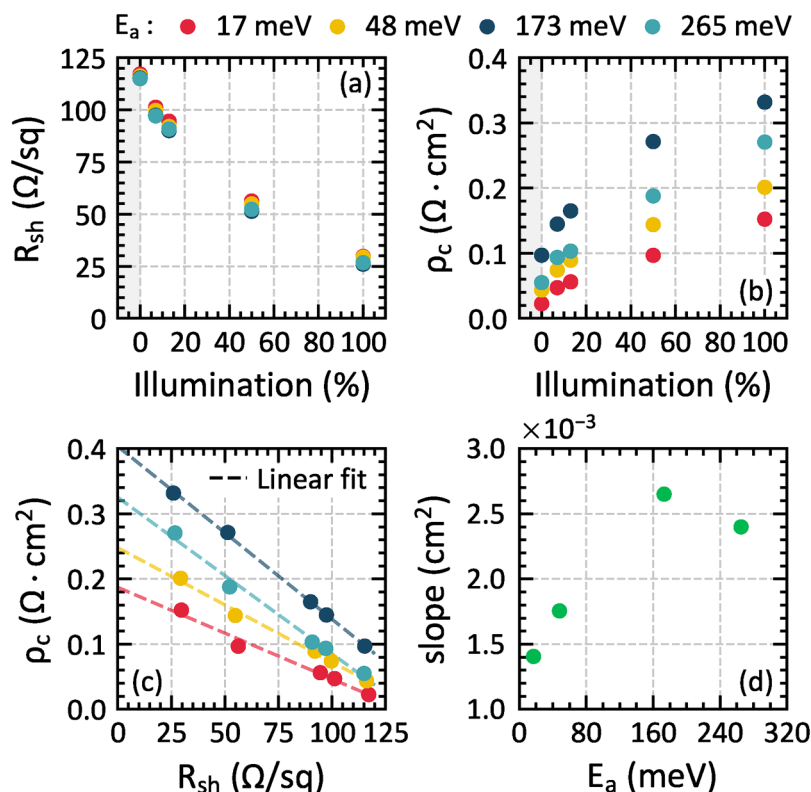


FIG. 13. (a) and (b) R_{sh} and ρ_c as a function of the illumination intensity. (c) ρ_c as a function of R_{sh} of a different n-type thin silicon layer with activation energy ranging from 17 to 265 meV as well as the linear fits and (d) the corresponding slope as a function of the activation energy.

TABLE III. Average experimental values of R_{sh} , N_e , and ΔN_e of the different shells under study.

Illumination	R_{sh} (Ω/sq)	N_e (cm^{-3})	ΔN_e (cm^{-3})
Dark	116	1.64×10^{15}	0
7%	99	1.94×10^{15}	2.96×10^{14}
13%	92	2.09×10^{15}	4.55×10^{14}
50%	54	3.71×10^{15}	2.07×10^{15}
100%	28	7.60×10^{15}	5.96×10^{15}

of 173 meV presents the highest illumination sensitivity because of a lower dark electron accumulation. From these considerations, it is also important to discuss the drop of the slope for E_a of 265 meV. This drop suggests that despite a higher E_a , its illumination impact is smaller than the shell featuring E_a of 173 meV. This highlights the fact that, as already well known, E_a is not the only parameter ruling the accumulation and the illumination response in SHJ solar cells. Other key parameters, especially defect density, are involved and must be considered.^{18,19} In addition, it is observed that the shells with E_a of 265 and 48 meV feature similar ρ_c in the dark (0.05 and $0.04 \Omega \text{ cm}^2$, respectively) but different slopes of 2.4×10^{-3} and $1.8 \times 10^{-3} \text{ cm}^2$, respectively. This result highlights the relevance of our approach: in addition to comparing shells based on their resistive losses, it is possible to compare their response to the illumination. A second major observation is that for all E_a under study, the ρ_c value obtained under MPP conditions (here, for $\Delta N_e = 2.07 \times 10^{15}$ and R_{sh} of $54 \Omega/\text{sq}$) is between 0.07 and $0.17 \Omega \text{ cm}^2$ higher than the one obtained in the dark. Hence, the difference between the induced FF loss calculated at an illumination corresponding to around MPP and the one in the dark is between 0.35 and $0.85\%_{\text{abs}}$.⁴⁰ Thus, to have effective n-type contact stacks, a small dark contact resistivity and/or the smallest slope must be targeted so that the contact is as less as possible sensitive to illumination. This again pinpoints the pertinence of our method to assess the quality of the carrier transport under the conditions experienced in the field by solar cells, where injected carriers play an important role.

D. Edge recombination and its impact on contact resistivity measurement

Figure 14(a) plots the simulated $R_{sh}(x)$ profiles present below the TLM pad for the different illuminations. These profiles are defined; for example, the $R_{sh_{\text{eq}}}$ obtained with Eq. (3) is seen matching the values corresponding to the experimental R_{sh} data for the case of $E_a = 265$ meV (shell 1) presented in Table III. It is observed that $R_{sh}(x)$ is significantly affected by edge recombination: a strong increase at the TLM pad edges is clearly visible. This is due to a strong decrease in the excess carrier concentration from the middle of the pad to its edges induced by the edge recombination. Then, the contact resistivity profile ($\rho_c(x)$) was calculated considering the experimental dependence between ρ_c and the illuminated R_{sh} presented in Sec. III C. For each $R_{sh}(x)$ profile, the $\rho_c(x)$ profile is calculated for the case of $E_a = 256$ meV using the experimental dependence presented in Fig. 13(c) and is plotted in Fig. 14(b). Following the experimental pieces of evidence in Sec. III C, it is observed that the higher the R_{sh} , the lower ρ_c . Thus, a significantly smaller value of ρ_c is observed at the edges compared with the middle of the pad. Then, using Eqs. (4)–(7), TLM computation is performed with the dependence of $R_{\text{TLM}k}$ as a function of the interpad distance of gap k . The output values of ρ_c are presented in Table IV and compared with the experimental ones. It is observed that both experimental and computed values are close: their difference spans from -5.8% to 3.3% . This difference is representative of the global error calculated for all the n-type multilayers under study, which was found to be $\pm 5.8\%$. This demonstrates that considering the spatial distribution of $R_{sh}(x)$, in addition to the experimental linear dependence of ρ_c with the R_{sh} , the final values obtained are close to the ones extracted with the standard TLM computation considering a homogeneous R_{sh} . In addition, note that PC1D simulation ignores the conduction of free carriers inside the thin silicon/TCO stacks that were recently demonstrated to provide efficient lateral transport when combined with the c-Si(n) bulk.⁴² If this effect proves relevant for the samples investigated in this paper, it will lead to a

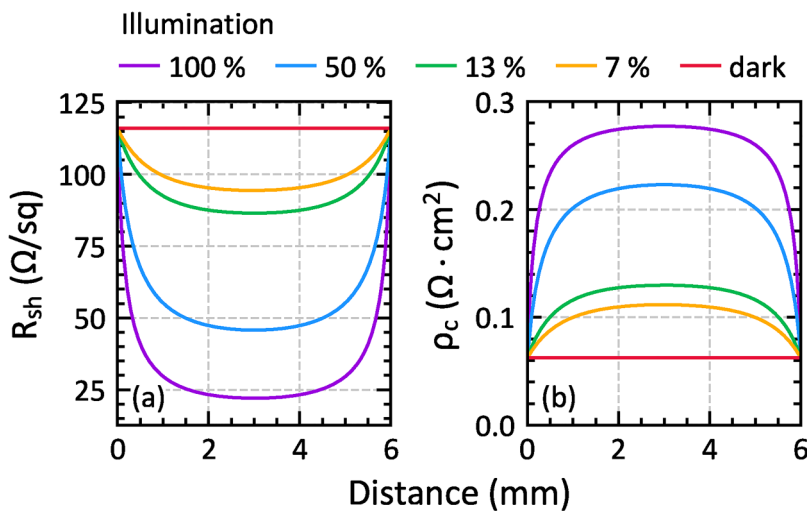
**FIG. 14.** Equivalent electron sheet resistance profile (a) and contact resistivity profile (b) below the TLM pad width considering the different illumination, for the case of $E_a = 265$ meV (shell 1).

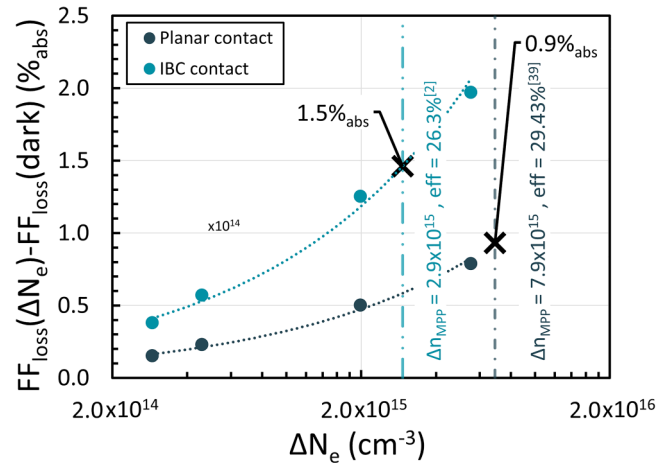
TABLE IV. Experimental and computed value of ρ_c for the case of $E_a = 265$ meV (shell 1) and for the different illumination intensities.

Illumination	ρ_c ($\Omega \text{ cm}^2$)		Difference	Error (%)
	Experimental	Computed		
7%	1.07×10^{-1}	1.01×10^{-1}	-6.22×10^{-3}	-5.8
13%	1.16×10^{-1}	1.16×10^{-1}	4.06×10^{-4}	0.4
50%	1.96×10^{-1}	2.03×10^{-1}	6.43×10^{-3}	3.3
100%	2.75×10^{-1}	2.67×10^{-1}	-8.17×10^{-3}	-3.0

homogenization of the R_{sh} profile and then mitigate the edge effects. The impact of the non-homogeneous R_{sh} on the final extracted value of ρ_c using the standard TLM computation is then limited. Thus, our method to extract ρ_c under variable illuminations yields a negligible error and is, therefore, accurate enough to study the ρ_c evolution as a function of the excess carrier concentration. Note that the TLM pad width can be increased to reduce the error induced by the edge effect. However, by doing so, the silver pad conductivity must be adapted to not provide any additional error. Indeed, it has been demonstrated in Ref. 38 that the measurement of ρ_c depends significantly on the TLM pad width for a fixed silver pad conductivity, leading to a rise in the error in the measurement of ρ_c with the width augmentation.

E. Outlook

As highlighted in the introduction of this paper, solar cells using passivating contact are nowadays achieving high conversion efficiency and approaching their intrinsic efficiency limit. In this quest for maximal efficiency, the higher the device performances, the more difficult it is to identify ways for effecting further improvements. The method presented in this work may insightfully complete the already existing ones, such as SunsVoc at a very high injection⁴³ or the works presented in Refs. 9 and 26, to help further understand and study the electrical transport in solar cells with the aim of guiding their actual efficiency improvement. In addition, this method might prove particularly relevant considering the augmentation of the injection level at MPP that goes along with the continuous increase in solar cell efficiencies. Nowadays, record-breaking SHJ devices present MPP injection levels around $2.9 \times 10^{15} \text{ cm}^{-3}$,² and the theoretical limit of single junction devices presented by Richter⁴⁴ predicts an MPP injection level up to around $7.9 \times 10^{15} \text{ cm}^{-3}$. Therefore, the higher the MPP injection, the higher will be the difference between the contact resistivity measured in the dark and its actual value at MPP for a given shell. This is illustrated in Fig. 15, which plots the FF loss difference between different injection conditions and in the dark, considering the linear dependence of the ρ_c to the R_{sh} of shell 3 featuring an E_a of 48 meV [Fig. 13(c)]. The injection considered are those listed in Table III. The cases of planar and localized IBC contacts are studied assuming an IBC n-type contact fraction of 40%.⁴ The FF loss difference will actually be about 0.9%_{abs} considering the theoretical limit of single junction devices as presented by Richter,⁴⁴ and it will go up to about 1.5%_{abs} for the case of Kaneka's record IBC device.² This demonstrates that the higher

**FIG. 15.** FF loss difference between different injection levels and in the dark, considering the linear dependence of the contact resistivity on the injection of shell 3 for a planar contact (gray) and an IBC (blue) contact. The two dotted lines are guides to the eyes to follow both FF loss evolutions.

the MPP injection, the less relevant the contact resistivity measured in the dark will be for an accurate FF loss breakdown. Note that in both cases, the contribution of the c-Si(n) bulk to the final FF loss decreases with the illumination augmentation as its resistivity is reduced. Indeed, a reduction in the FF loss difference between MPP injection and in the dark up to $-0.18\%_{\text{abs}}$ is expected for planar contacts and up to $-1.02\%_{\text{abs}}$ for IBC contact, which will partly counterbalance the augmentation of the FF loss induced by the increase of ρ_c . Last but not least, it is important to remind ourselves that so far we have focused on the influence of only E_a . Yet, it is well known that E_a is not the only parameter ruling the accumulation and the illumination response in SHJ solar cells. Other key parameters, especially defect density, are involved and must be considered.^{18,19} Overall, our method provides valuable information about the global illumination response of the electron-collecting part of a shell regardless of the individual parameters of each of its sub-components and can then be further generalized to the investigation of other parameters than E_a . Furthermore, we think our approach to be of general validity and to be equally applicable to investigate shells based on technologies other than SHJ, such as the POLO and the TOPCon.

V. CONCLUSION

In this contribution, we presented a new methodology to characterize the electrical transport quality of SHJ solar cells. First, we introduced the terminology of shell to provide a generalized and unambiguous description of contacts in solar cells allowing to accurately investigate the electrical losses affecting SHJ solar cells. Second, we presented the TLM measurement under variable illumination, which was demonstrated to be a relevant characterization method to investigate and assess the carrier transport quality of n-type SHJ contact stacks. This method

revealed a strong dependence of ρ_c as a function of the c-Si bulk R_{sh} induced by different injected carrier densities. The importance of considering the MPP condition to measure ρ_c in order to study the impact on the transport losses and, thus, on the real value of FF of solar cells is also demonstrated. In addition, this method showed that different n-type contact stacks featuring various E_a are impacted differently by illumination. These results were supported by TCAD simulation with a particular focus on the E_a of n-type thin silicon layers to change the accumulation at the c-Si (n)/a-Si:H(i) interface. In addition, the different limitations of this method, namely, the non-ohmic behavior induced by TLM applied voltage and edge recombination, were elucidated. Finally, this study presented the first results and investigations of the impact of the illumination on the ρ_c value and provided the first insights into the involved physical phenomena. However, the global description and understanding of the physical phenomena responsible for the linear rise of ρ_c with the decrease of R_{sh} , induced by the illumination increase, are still matters of investigation.

ACKNOWLEDGMENTS

A big and warm thanks to P. Martens for his valuable help and guidance regarding the Python scripts written for this work, E. Wild for her help with the first data treatment, R. Mottet and L. Antognini for their fruitful discussions, as well as J. Cattin for providing solar cell sketches. The authors also acknowledge funding provided by the SNSF SHAMAN under Grant Agreement No. 200021_192310.

APPENDIX: NON-OHMIC BEHAVIOR

In this section, the appearance of the non-ohmic regime due to the drift of the free carriers induced by the voltage applied between two consecutive TLM pads is explained in more detail. This phenomenon leads to a non-homogeneous carrier density and, thus, to a variation in the wafer R_{sh} below the TLM pads and the gap in-between. The latter breaks one of the fundamental hypotheses of TLM measurement, which states that the R_{sh} must be homogeneous inside the conductive layer, i.e., inside the c-Si(n) bulk here. Our simple calculations reveal that the higher the voltage bias applied between two TLM pads, the higher the global resistance seen by the TLM current when flowing through the conductive layer [i.e., the c-Si(n) bulk], leading then to a non-ohmic I-V behavior. Under illumination, free holes and electrons are generated inside the c-Si(n) bulk. First, considering zero applied TLM voltage between two pads, i.e., $\Delta U = 0$ V voltage bias, the electrons are homogeneously distributed inside the c-Si(n) bulk along the distance L , and their density equals $n_{0e} + \Delta n_e$, with n_{0e} the bulk doping density, everywhere within the sample bulk (see Fig. 11). We then have

$$R_{shj} = \frac{\rho_j}{d}, \sigma_j = q\mu_j n_j, \rho_j = \frac{1}{q\mu_j n_j}, \quad (\text{A1})$$

with the index j standing for electron (e) or hole (h), d the wafer thickness, σ the conductivity, ρ the resistivity, and μ the mobility. These three parameters are then homogeneous inside the wafer, and then the resistive contribution R of the wafer to the total

resistance measured between two pads is also homogeneous with

$$U = RI, \quad I = \frac{U}{R} = U \times \Sigma, \quad (\text{A2})$$

$$\Sigma_j = \frac{1}{R_j} = \frac{\sigma_j}{L} = \frac{q\mu_j n_j}{L}. \quad (\text{A3})$$

Here, U is the voltage, I is the current between two TLM pads, and Σ is the conductance (the inverse of R),

$$\Sigma_{0V} \propto \frac{n_0 + \Delta n}{L}, \quad (\text{A4})$$

$$\Sigma_{\alpha V} \propto \frac{1}{\frac{L}{2} + \frac{L}{2}} = \frac{n_0(n_0 + 2\Delta n)}{L(n_0 + \Delta n)}. \quad (\text{A5})$$

Comparing both parameters, we get

$$\frac{\Sigma_{\alpha V}}{\Sigma_{0V}} = \frac{n_0^2 + 2\Delta n n_0}{n_0^2 + 2\Delta n n_0 + \Delta n^2} < 1, \quad (\text{A6})$$

$$\frac{R_{0V}}{R_{\alpha V}} = \frac{n_0^2 + 2\Delta n n_0}{n_0^2 + 2\Delta n n_0 + \Delta n^2} < 1. \quad (\text{A7})$$

Thus, from the computed equivalent resistance of the sample bulk seen by the electrons in the 0 V and the α V cases (R_{0V} and $R_{\alpha V}$, respectively), it turns out that $R_{0V} < R_{\alpha V}$. Said differently, the wafer resistance is depending on the applied bias U , i.e., $R = R(U)$. Hence, the higher the TLM applied bias, the higher the total resistance seen by the TLM current between two TLM pads ($R_{\alpha V}$ gets larger and larger than R_{0V}). This explains the non-Ohmic shape of the IV curve obtained between two TLM pads measured under illumination. Therefore, at low voltages, a linear I-V regime is still present, because the drift effect is small, but as soon as the voltage increases, the non-ohmic I-V behavior appears, then stabilizes at high voltages to a second linear I-V regime. This second linear regime features a higher slope than the first linear one, evidencing the increase of the c-Si global resistance with the voltage (see Fig. 16). In addition, it is observed that with the increase of the illumination, and thus of Δn_e , the applied voltage required to reach a given current is smaller, i.e., the global resistance is smaller, as the R_{sh} of the c-Si(n) bulk decreases with the Δn_e increase (see Fig. 16). Importantly, because of the fact that, for a given TLM bias, both TLM pads feature two different R_{sh} below them, the ρ_c is not equal between the two pads, making impossible to perform TLM computation. In addition, the resulting resistance between the two TLM pads varies with the TLM bias voltage, but this resistive effect is negligible compared with the wafer R_{sh} variation with the TLM bias voltage.

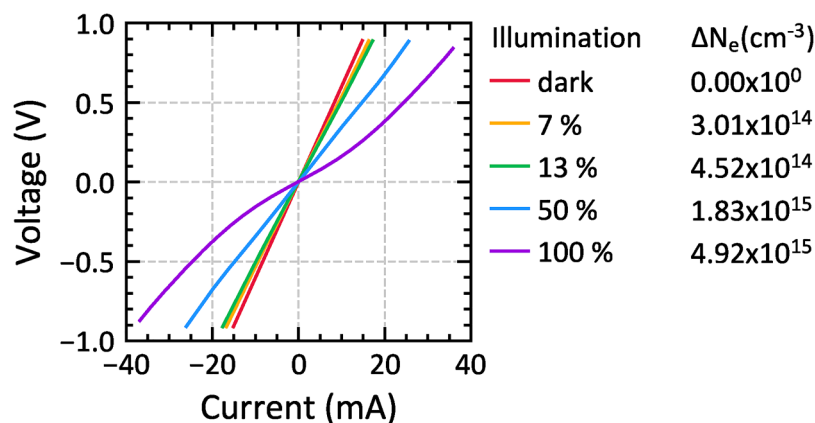


FIG. 16. I-V characteristics of shell 2 as a function of illumination, for the TLM gap of 2.5 mm. The injected electron densities are also reported along with the corresponding illuminations.

DATA AVAILABILITY

The data that support the findings of this study are available within the article and from the corresponding author upon reasonable request.

REFERENCES

- ¹A. Cuevas, T. Allen, J. Bullock, Y. Wan, D. Yan, and X. Zhang, "Skin care for healthy silicon solar cells," in *2015 IEEE 42nd Photovoltaics Special Conference PVSC 2015, No. 1* (IEEE, 2015), pp. 1–6.
- ²K. Yoshikawa *et al.*, "Silicon heterojunction solar cell with interdigitated back contacts for a photoconversion efficiency over 26%," *Nat. Energy* **2**(5), 17032 (2017).
- ³F. Haase *et al.*, "Laser contact openings for local poly-Si-metal contacts enabling 26.1%-efficient POLO-IBC solar cells," *Sol. Energy Mater. Sol. Cells* **186**, 184–193 (2018).
- ⁴P. Procel, G. Yang, O. Isabella, and M. Zeman, "Theoretical evaluation of contact stack for high efficiency IBC-SHJ solar cells," *Sol. Energy Mater. Sol. Cells* **186**, 66–77 (2018).
- ⁵U. Wurfel, A. Cuevas, and P. Wurfel, "Charge carrier separation in solar cells," *IEEE J. Photovoltaics* **5**(1), 461–469 (2015).
- ⁶L.-L. Senaud *et al.*, "Aluminium-doped zinc oxide rear reflectors for high-efficiency silicon heterojunction solar cells," *IEEE J. Photovoltaics* **9**(5), 1217–1224 (2019).
- ⁷M. Tanaka *et al.*, "Development of new a-Si/c-Si heterojunction solar cells: ACJ-HIT (artificially constructed junction- heterojunction with intrinsic thin-layer)," *Jpn. J. Appl. Phys.* **31**(11R), 3518–3522 (1992).
- ⁸P. Würfel, *Physics of Solar Cells: From Principles to New Concepts* (Wiley-VCH, 2005).
- ⁹A. Fell, J. Schön, M. C. Schubert, and S. W. Glunz, "The concept of skins for silicon solar cell modeling," *Sol. Energy Mater. Sol. Cells* **173**, 128–133 (2017).
- ¹⁰E. Yablonovitch, T. Gmitter, R. M. Swanson, and Y. H. Kwark, "A 720 mV open circuit voltage SiO_x/c-Si:SiO_x double heterostructure solar cell," *Appl. Phys. Lett.* **47**(11), 1211–1213 (1985).
- ¹¹F. Feldmann, M. Bivour, C. Reichel, M. Hermle, and S. W. Glunz, "Passivated rear contacts for high-efficiency n-type Si solar cells providing high interface passivation quality and excellent transport characteristics," *Sol. Energy Mater. Sol. Cells* **120**(Pt. A), 270–274 (2014).
- ¹²U. Römer *et al.*, "Recombination behavior and contact resistance of n⁺ and p⁺ poly-crystalline Si/mono-crystalline Si junctions," *Sol. Energy Mater. Sol. Cells* **131**, 85–91 (2014).
- ¹³P. Koswatta, M. Boccard, and Z. Holman, "Carrier-selective contacts in silicon solar cells," in *2015 IEEE 42nd Photovoltaics Special Conference PVSC 2015, No. 2* (IEEE, 2015), pp. 13–16.
- ¹⁴A. Richter *et al.*, "Both sides contacted silicon solar cells: Option for approaching 26% efficiency," in *36th European Photovoltaics and Solar Energy Conference and Exhibition* (EUPVSEC, 2019), pp. 90–95.
- ¹⁵E. T. Roe, K. E. Egelhofer, and M. C. Lonergan, "Exchange current density model for the contact-determined current-voltage behavior of solar cells," *J. Appl. Phys.* **125**(22), 225302 (2019).
- ¹⁶A. Onno, C. Chen, P. Koswatta, M. Boccard, and Z. C. Holman, "Passivation, conductivity, and selectivity in solar cell contacts: Concepts and simulations based on a unified partial-resistances framework," *J. Appl. Phys.* **126**(18), 183103 (2019).
- ¹⁷P. Procel *et al.*, "On the correlation between contact resistivity and high efficiency in (IBC-) SHJ solar cells," in *Proceedings of the 36th European Photovoltaic Solar Energy Conference and Exhibition* (2019) (EUPVSEC, 2019), pp. 251–254.
- ¹⁸R. Varache, J. P. Kleider, W. Favre, and L. Korte, "Band bending and determination of band offsets in amorphous/crystalline silicon heterostructures from planar conductance measurements," *J. Appl. Phys.* **112**(12), 123717 (2012).
- ¹⁹T. F. Schulze, L. Korte, E. Conrad, M. Schmidt, and B. Rech, "Electrical transport mechanisms in a-Si:H/c-Si heterojunction solar cells," *J. Appl. Phys.* **107**(2), 023711 (2010).
- ²⁰M. Jeong, P.-M. Solomon, S. E. Laux, H.-S. P. Wong, and D. Chidambarrao, "Comparison of raised and Schottky source/drain MOSFETs using a novel tunneling contact model," in *International Electron Devices Meetings 1998 Technical Digest (Catalogue No. 98CH36217)* (IEEE, 1998), pp. 733–736.
- ²¹E. O. Kane, "Theory of tunneling," *J. Appl. Phys.* **32**, 83–91 (1961).
- ²²F. Jiménez-Molinos, F. Gámiz, A. Palma, P. Cartujo, and J. A. López-Villanueva, "Direct and trap-assisted elastic tunneling through ultra-thin gate oxides," *J. Appl. Phys.* **91**(8), 5116–5124 (2002).
- ²³D. B. M. Klaassen, "A unified mobility model for device simulation—I. Model equation and concentration dependence," *Solid State Electron.* **35**(7), 953–959 (1992).
- ²⁴D. B. M. Klaassen, "A unified mobility model for device simulation-II. Temperature dependence of carrier mobility and lifetime," *Solid State Electron.* **35**(7), 961–967 (1992).
- ²⁵A. Cuevas *et al.*, "Carrier population control and surface passivation in solar cells," *Sol. Energy Mater. Sol. Cells* **184**, 38–47 (2018).
- ²⁶R. Brendel and R. Peibst, "Contact selectivity and efficiency in crystalline silicon photovoltaics," *IEEE J. Photovoltaics* **6**(6), 1413–1420 (2016).
- ²⁷A. Descœudres *et al.*, "Improved amorphous/crystalline silicon interface passivation by hydrogen plasma treatment," *Appl. Phys. Lett.* **99**(12), 2009–2012 (2011).
- ²⁸A. Descœudres *et al.*, "Advanced silicon thin films for high-efficiency silicon heterojunction-based solar cells," in *2017 IEEE 44th Photovoltaics Special Conference (PVSC)*, Washington, DC (IEEE, 2017), pp. 50–55.

- ²⁹L.-L. Senaud *et al.*, “Decoupling bulk and interface properties in the shells of silicon heterojunction solar cells,” in *Oral Present. SiliconPV* (Silicon PV, 2019).
- ³⁰L.-L. Senaud *et al.*, “Bottom-up vs top-down approaches for identifying and mitigating the transport losses in high-efficiency silicon heterojunction solar cells,” in *Oral Presentation EUPVSEC* (EUPVSEC, 2019).
- ³¹A. Shah, C. Ballif, W. Beyer, F. Finger, and H. Schade, *Thin-Film Silicon Solar Cells* (EPFL Press, 2010).
- ³²D. S. Ginley, H. Hosono, and D. C. Paine, *Handbook of Transparent Conductors* (Springer, Boston, MA, 2011).
- ³³S. Eideloth and R. Brendel, “Analytical theory for extracting specific contact resistances of thick samples from the transmission line method,” *IEEE Electron Device Lett.* **35**(1), 9–11 (2014).
- ³⁴Sentaurus, Sentaurus Device User Guide (Synopsis, 2015).
- ³⁵A. Klein *et al.*, “Transparent conducting oxides for photovoltaics: Manipulation of Fermi level, work function and energy band alignment,” *Materials* **3**(11), 4892–4914 (2010).
- ³⁶P. Procel *et al.*, “The role of heterointerfaces and subgap energy states on transport mechanisms in silicon heterojunction solar cells,” *Prog. Photovoltaics Res. Appl.* **28**, 935–945 (2020).
- ³⁷D. A. Clugston and P. A. Basore, “PC1D version 5: 32-bit solar cell modeling on personal computers,” in *Conference Record of the IEEE Photovoltaics Special Conference* (IEEE PVSC, 1997), pp. 207–210.
- ³⁸S. Guo, G. Gregory, A. M. Gabor, W. V. Schoenfeld, and K. O. Davis, “Detailed investigation of TLM contact resistance measurements on crystalline silicon solar cells,” *Sol. Energy* **151**, 163–172 (2017).
- ³⁹D. Lachenal *et al.*, “Optimization of tunnel-junction IBC solar cells based on a series resistance model,” *Sol. Energy Mater. Sol. Cells* **200**, 110036 (2019).
- ⁴⁰D. Pysch, A. Mette, and S. W. Glunz, “A review and comparison of different methods to determine the series resistance of solar cells,” *Sol. Energy Mater. Sol. Cells* **91**(18), 1698–1706 (2007).
- ⁴¹R. H. Cox and H. Strack, “Ohmic contacts for GaAs devices,” *Solid State Electron.* **10**(12), 1213–1218 (1967).
- ⁴²J. Cattin, J. Haschke, C. Ballif, and M. Boccard, “Influence of local surface defects on the minority-carrier lifetime of passivating-contact solar cells influence of local surface defects on the minority-carrier lifetime of passivating-contact solar cells,” *Appl. Phys. Lett.* **116**(11), 113901 (2020).
- ⁴³M. Bivour, M. Reusch, F. Feldmann, M. Hermle, and S. Glunz, “Requirements for carrier selective silicon heterojunctions,” in *Proceedings of the 24th Workshop on Crystalline Silicon Solar Cells & Modules: Materials and Processes* (2014), pp. 1–9.
- ⁴⁴A. Richter, M. Hermle, and S. W. Glunz, “Reassessment of the limiting efficiency for crystalline silicon solar cells,” *IEEE J. Photovoltaics* **3**(4), 1184–1191 (2013).